Water Penetration and Binding to Ferric Myoglobin[†]

Wenxiang Cao, James F. Christian, Paul M. Champion,* Florin Rosca, and J. Timothy Sage*

Department of Physics and Center for Interdisciplinary Research on Complex Systems, Northeastern University, Boston, Massachusetts 02115

ABSTRACT: Flash photolysis investigations of horse heart metmyoglobin bound with NO ($Mb^{3+}NO$) reveal the kinetics of water entry and binding to the heme iron. Photodissociation of NO leaves the sample in the dehydrated Mb^{3+} (5-coordinate) state. After NO photolysis and escape, a water molecule enters the heme pocket and binds to the heme iron, forming the 6-coordinate aquometMb state ($Mb^{3+}H_2O$). At longer times, NO displaces the H_2O ligand to reestablish equilibrium. At 293 K, we determine a value $k_w \approx 5.7 \times 10^6$ s^{-1} for the rate of H_2O binding and estimate the H_2O dissociation constant as 60 mM. The Arrhenius barrier height $H_w = 42 \pm 3$ kJ/mol determined for H_2O binding is identical to the barrier for CO escape after photolysis of $Mb^{2+}CO$, within experimental uncertainty, consistent with a common mechanism for entry and exit of small molecules from the heme pocket. We propose that both processes are gated by displacement of His-64 from the heme pocket. We also observe that the bimolecular NO rebinding rate is enhanced by 3 orders of magnitude both for the H64L mutant, which does not bind water, and for the H64G mutant, where the bound water is no longer stabilized by hydrogen bonding with His-64. These results emphasize the importance of the hydrogen bond in stabilizing H_2O binding and thus preventing NO scavenging by ferric heme proteins at physiological NO concentrations.

Myoglobin (Mb)[1] is a reversible oxygen (O_2) carrying and storage protein found in muscle cells and is one of the simplest heme proteins. Mb has been studied extensively as a model for exploring the relationship between protein structure, dynamics, and function (*1*). In addition to O_2, the ferrous heme iron (Fe) in myoglobin (Mb^{2+}) can bind other diatomic ligands, such as carbon monoxide (CO) and nitric oxide (NO). NO is found in vivo and regulates various physiological functions including blood pressure (*2, 3*), platelet aggregation, and neurotransmission (*4, 5*). Because of the physiological significance of reversible binding of diatomic ligands, the kinetics for O_2, CO, and NO binding to Mb^{2+} have been studied in detail (*6, 7*). Moreover, water (H_2O), which is abundant in the surrounding solvent and protein structure, can also bind to the *ferric* heme iron of oxidized myoglobin (Mb^{3+}) as a weak field ligand (*8*). Water molecules participate in many biomolecular processes (*9–12*). The interaction of water molecules with biomolecules has been studied intensively, both theoretically (*13, 14*) and experimentally (*9, 15*), but water transport through the protein interior remains poorly understood.

In Mb^{2+}, H_2O does not bind to the ferrous heme Fe, but can hydrogen bond to His-64 in the distal heme pocket (*8*). When other ligands such as O_2, CO, or NO bind to the ferrous iron atom in Mb^{2+}, the distal pocket water molecule is displaced. The displacement of the H_2O molecule upon

O_2/CO/NO binding has been proposed to influence ligand rebinding kinetics (*6, 16–18*), although the low occupancy of the distal H_2O in the high-resolution X-ray structure (*19*) of Mb^{2+} at room temperature raises questions about the energetic significance of this effect. Spectroscopic signatures of the distal pocket water (*18, 20, 21*) in Mb^{2+} are too subtle to conveniently monitor H_2O kinetics. In Mb^{3+}, on the other hand, the large optical absorption difference (Figure 1) between 6-coordinate (*8*) water-bound heme Fe^{3+} and the 5-coordinate heme Fe^{3+} makes it possible to monitor water binding kinetics directly. In this work, we present laser flash photolysis experiments on metmyoglobin bound with NO ($Mb^{3+}NO$) in buffer solution and investigate the time scale and possible pathway for H_2O entry into the heme pocket. Although geminate water binding to a nonequilibrium state of Mb^{2+} at low temperature has been reported (*22–24*), the rate of H_2O entry into the heme pocket of Mb near physiological temperatures has not been studied previously.

Our results show that after NO is dissociated, water enters the heme pocket, binds to the heme Fe^{3+}, and is subsequently displaced during the bimolecular rebinding of NO. NO association with H64L and H64G mutants is approximately 3 orders of magnitude faster than in the native protein, suggesting that H-bond stabilization of bound H_2O by His-64 may prevent scavenging of NO by ferric heme proteins. The water entry rate is found to be $k_w = 5.7 \times 10^6$ s^{-1} at 293 K, with an associated Arrhenius barrier $H_w = 42 \pm 3$ kJ/mol. The barrier height for CO escape from Mb^{2+} is identical within experimental uncertainty, consistent with a common mechanism for entry and exit of small molecules from the heme pocket. We suggest that His-64 plays a dynamic role in controlling the access of small molecules to the binding site.

* Corresponding authors. J.T.S.: e-mail, jtsage@neu.edu; phone, (617)-373-2908; fax, (617)-373-2943. P.M.C.: e-mail, champ@neu.edu; phone, (617)-373-2918; fax, (617)-373-2943.

[1] Abbreviations: Mb, myoglobin; Mb^{2+}, reduced myoglobin; Mb^{3+}, oxidized myoglobin; MEM, maximum entropy method; LS, least squares; BPTI, bovine pancreatic trypsin inhibitor.

EXPERIMENTAL PROCEDURES

Sample Preparation. Native horse heart myoglobin was purchased from Sigma Chemical Co. Sperm whale myoglobin mutants H64L and H64G, expressed from a synthetic gene in *Escherichia coli* (*25*), were obtained from Prof. S. G. Sligar at the University of Illinois. $Mb^{3+}NO$ samples with the desired concentration (60−90 μM) were prepared in 0.067 M KH_2PO_4/Na_2HPO_4, pH 6.44, buffer solution (*26*) to retard autoreduction and then transferred to 1 mm quartz cuvettes sealed by rubber septa. Samples were degassed by repeated evacuation and flushing with Ar or by continuous flushing with Ar for more than 20 min. The NO gas (99.0% pure, Matheson) was bubbled through 0.1 M NaOH solution (*27−30*), and then through buffer solution, and finally was introduced to degassed samples at a pressure of 1 atm for about 20 s. Samples prepared in this fashion were stable (against autoreduction to $Mb^{2+}NO$) for approximately 40 min at room temperature and for more than 1 h at 273 K. MbCO samples were prepared from horse metMb as previously described (*31*). All pH values were obtained using a Beckman Instruments Φ40 pH meter. Static absorption spectra were measured using a Hitachi U-3410 spectrophotometer.

Experimental Setup and Procedures. The flash photolysis experimental setup and procedures are similar to those reported previously (*32−34*) with the following minor changes. A cw beam produced by a universal arc lamp (Oriel Instruments, model 66021) and a 0.25 m monochromator (Oriel Instruments, model 77200) was used to probe the kinetic response of the sample at selected wavelengths. The signal is detected by a high-linearity low-noise photomultiplier (Hamamatsu, H6780) and recorded by a transient digitizer (LeCroy 9420). The laser pulse (10 ns, 532 nm), produced by a 10 Hz Nd-doped yttrium−aluminum−garnet (YAG) laser (Continuum Surelite I), is used to photolyze the sample. The pump pulse energy is typically 25 mJ.

The ultrafast pump−probe experimental setup is described in detail elsewhere (*35*). Briefly, 70 fs pump and probe pulses are generated by frequency doubling the output of a mode-locked Ti:Sapphire laser, and the arrival of the probe pulse at the sample is delayed with respect to the pump pulse by a variable optical delay line. Typical energies are 0.5 nJ per pump/probe pulse pair. Pump-induced changes in transmission as a function of delay time are measured in an "open band" configuration (*35*) by phase-sensitive detection of the probe beam intensity using a photodiode and a lock-in amplifier referenced to the pump modulation frequency.

Data Analysis. We use both a maximum entropy method (MEM) (*36−38*) and a global Levenberg−Marquardt non-linear least-squares (LS) method to analyze the kinetic data. To obtain the rate constants, the LS method simultaneously fits the experimentally observed absorbance changes, $\Delta A(t)$, recorded at one or more wavelengths to a function of the form

$$\Delta A(t) = I_g e^{-(k_g t)^\beta} - I_w e^{-k_w t} + I_s e^{-k_s t} \qquad (1)$$

The rates (k_g, k_w, k_s) are constrained to have the same value at all wavelengths, while the amplitudes (I_g, I_w, I_s) vary independently. (Below, we will identify the three processes g, w, and s with geminate NO rebinding, bimolecular H_2O
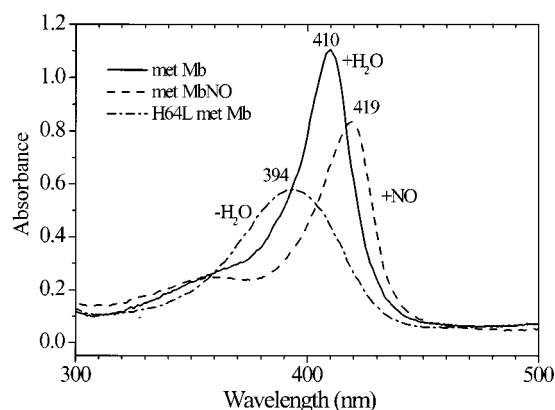

FIGURE 1: Absorption spectra of the equilibrium 6-coordinate ligation states $Mb^{3+}H_2O$ (solid line) and $Mb^{3+}NO$ (dashed line) of native metMb, along with the spectrum of the H64L mutant (Mb^{3+}, dash−dot line). H64L is 5-coordinate in the ferric oxidation state, analogous to the transient photoproduct created when native Mb^{3+}-NO is dissociated. The key experimental wavelength is near 410 nm, where we expect to see the absorbance increase when H_2O binds, and subsequently decrease when NO replaces H_2O. At 390 and 419 nm, the absorbance change (ΔA) monotonically decreases (at 390 nm) or increases (at 419 nm) during the ligand binding process.

association, and bimolecular NO rebinding to Mb^{3+}.) Alternatively, MEM describes the observed data using a logarithmic rate distribution $f(\log k)$, obtained by fitting the data with

$$\Delta A(t) = \int_0^\infty f(\log k) e^{-kt} \, d(\log k) \qquad (2)$$

For distributions $f(\log k)$ composed of a series of symmetric peaks, rate constants are then assigned to the peak values. We note that MEM analysis of a stretched exponential ($\beta < 1$ in eq 1) leads to a broad asymmetric distribution that contrasts with the sharply peaked symmetric distribution of a single exponential ($\beta = 1$). The inset in Figure 2a′ compares distributions resulting from MEM fits to synthetic data with $\beta = 0.5$ and $\beta = 1$. For $Mb^{3+}NO$ kinetics, LS fits to eq 1 with $\beta = 1$ yielded rate constants that agreed with values obtained using MEM, within the estimated 10−15% error margin. Rate constants for $Mb^{2+}CO$ were obtained using the LS method, with $I_w = 0$ and $\beta = 0.5$ in eq 1.
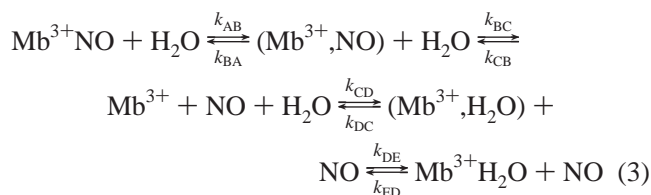
RESULTS

Figure 1 shows absorption spectra of the water-ligated ($Mb^{3+}H_2O$) and NO-ligated ($Mb^{3+}NO$) states of native metMb in the Soret band region, along with the spectrum of a H64L metMb mutant (Mb^{3+}) with the same concentration. The H64L mutant is 5-coordinate in the ferric oxidation state (*8, 39*) and is used here to simulate the transient 5-coordinate photoproduct (*28, 40, 41*) created when NO has been photolyzed, but the water has not yet bound to the Fe coordination site vacated by NO. For monitoring H_2O kinetics, the key experimental wavelength is the isosbestic point between $Mb^{3+}NO$ and 5-coordinate H64L metMb, which is located near the maximum absorbance of native metMb at 410 nm. From Figure 1, we expect that near 410 nm, the absorbance will first increase, when H_2O enters the heme pocket and binds to Fe^{3+} ($Mb^{3+} \rightarrow Mb^{3+}H_2O$), and later decrease, when NO replaces H_2O ($Mb^{3+}H_2O \rightarrow Mb^{3+}NO$). If we monitor at 390 and 419 nm, we will observe

a monotonic absorbance decrease (at 390 nm) or increase (at 419 nm) during the entire ligand binding (H_2O) and replacement (NO) process.

The left panels in Figure 2 show absorbance changes [$\pm\Delta A(t)$] following photolysis of native horse heart $Mb^{3+}NO$ at 293 K monitored at 390, 410, and 419 nm. Although only 10% of the proteins are photolyzed by the 10 ns YAG pulse [compared to 3.6% measured by Hoshino et al. (40)], due to geminate rebinding on faster time scales (see below), we obtain excellent signal-to-noise at all wavelengths. At 410 nm (Figure 2b), we can see that the absorbance first increases and then decreases. On the other hand, at 390 nm (Figure 2a) and 419 nm (Figure 2c), the absorbance changes monotonically [note that Figure 2c plots $-\Delta A(t)$].

The nonmonotonic absorbance change at 410 nm demonstrates that there are at least three distinct optical species. We interpret the experimental results displayed in Figure 2 in terms of three optical states: $Mb^{3+}NO$, $Mb^{3+}H_2O$ (6-coordinate), and Mb^{3+} (photoproduct, 5-coordinate), according to the consecutive reaction scheme

$$Mb^{3+}NO + H_2O \underset{k_{BA}}{\overset{k_{AB}}{\rightleftharpoons}} (Mb^{3+},NO) + H_2O \underset{k_{CB}}{\overset{k_{BC}}{\rightleftharpoons}}$$

$$Mb^{3+} + NO + H_2O \underset{k_{DC}}{\overset{k_{CD}}{\rightleftharpoons}} (Mb^{3+},H_2O) +$$

$$NO \underset{k_{ED}}{\overset{k_{DE}}{\rightleftharpoons}} Mb^{3+}H_2O + NO \quad (3)$$

where $Mb^{3+}NO$ and $Mb^{3+}H_2O$ are the NO- and H_2O-bound states, (Mb^{3+},NO) or (Mb^{3+},H_2O) are 5-coordinate states with NO or H_2O in the protein interior but not bound to Fe^{3+}, and Mb^{3+} is the 5-coordinate state with an empty heme pocket. According to this model, we interpret the sequence of events as follows. After NO is photodissociated, the sample is in the 5-coordinate state (Mb^{3+},NO). From this transient state, most of the NO (about 90% at 293 K) directly rebinds geminately to the heme Fe^{3+} without leaving the protein. After the nongeminate fraction of NO escapes to the solvent, forming a relatively long-lived 5-coordinate state (Mb^{3+}), water molecules can enter and bind, forming the 6-coordinate aquometMb state $(Mb^{3+}H_2O)$. The increase of the absorbance at 410 nm corresponds to the binding of H_2O $(Mb^{3+} \rightarrow Mb^{3+}H_2O)$. The time scale for this process is on the order of 200 ns at 293 K according to the data in Figure 2. Finally, on millisecond time scales, NO displaces the bound H_2O, leading to the decrease in ΔA seen in Figure 2b $(Mb^{3+}H_2O \rightarrow Mb^{3+}NO)$.

The right panels in Figure 2 show rate distributions $f(\log k)$ that result from fitting the kinetic processes in corresponding left panels using the maximum entropy method (MEM). The peaks in the rate distributions are narrow, indicating that they represent single exponential decays (note inset in Figure 2a'). The $\approx 10^5$ s^{-1} rate of the minor component in Figure 2 increases with NO concentration, and may include bimolecular NO rebinding to ferrous Mb^{2+}, present as an impurity due to autoreduction of $Mb^{3+}NO$. Because its amplitude is small and it is well separated in time, it does not affect the rates determined for the major kinetic components. The negative peak in Figure 2b' corresponds to the increase of ΔA in Figure 2b, i.e., the
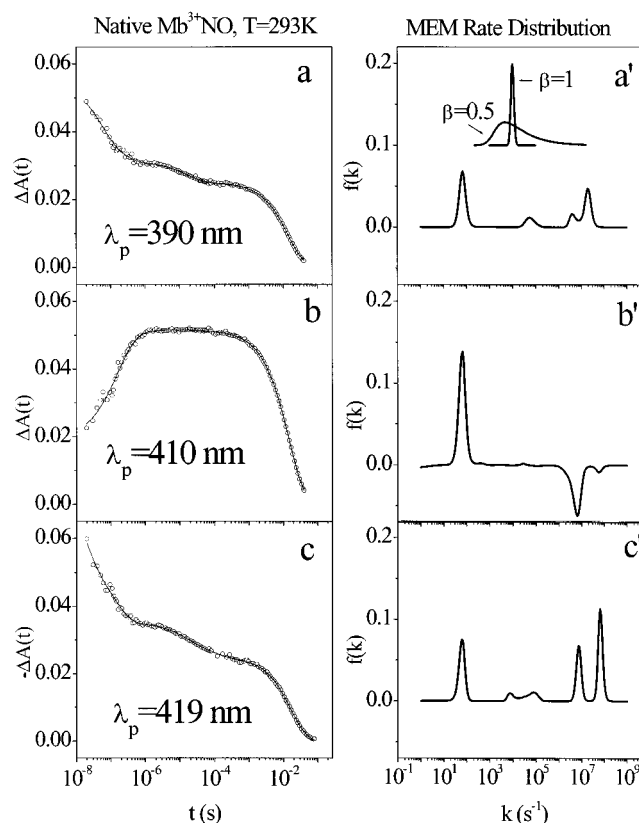

FIGURE 2: The left panels show absorbance changes (small circles) following photolysis of native horse heart $Mb^{3+}NO$ at 293 K monitored at (a) 390 nm, (b) 410 nm, and (c) 419 nm [note (c) is $-\Delta A$]. The solid lines are results of the MEM fits. In (b), the increase and subsequent decrease in absorbance correspond to the processes of H_2O binding followed by displacement of the bound H_2O by NO. The right panels show the MEM rate distributions $f(\log k)$ corresponding to the kinetic processes in the corresponding left panels. The negative peak in (b') represents a single exponential corresponding to the absorbance increase in (b) (H_2O entry and binding). For comparison, panel a' also shows rate distributions derived from MEM fits to the function $f(t) = e^{-(kt)^\beta}$ with $k = 10^4$ s^{-1} for single exponential ($\beta = 1$) and stretched exponential ($\beta = 0.5$) decays.

entry of H_2O into the heme pocket and its binding to the heme iron.

Ultrafast measurements (Figure 3) suggest that geminate NO rebinding is mostly completed on picosecond time scales. Figure 3 shows ultrafast measurements of the absorbance change at 410 and 419 nm following photolysis of native $Mb^{3+}NO$ at room temperature. The MEM rate distribution $f(\log k)$ reveals four exponential decays corresponding to kinetics (as well as a peak near 0.1 ps corresponding to coherence effects near zero delay). The time constants for the four exponential decays, calculated as the inverse $\tau = 1/k_{max}$ of the corresponding peak value in the rate distribution $f(\log k)$, are shown in Table 1. Analogous measurements on native horse heart metMb yield only the first two processes (about 0.6 and 5 ps, data not shown). On this basis, we identify the 0.6 and 4 ps processes (Figure 3, Table 1) with electronic decay and cooling processes of the photoexcited heme, which we report in detail elsewhere (35).

We attribute the 24 and 300 ps components to rapid photochemical processes. Geminate rebinding of NO by Mb^{3+} is undoubtedly the principal contribution. Geminate NO rebinding to Mb^{2+} (27), produced by autoreduction of a
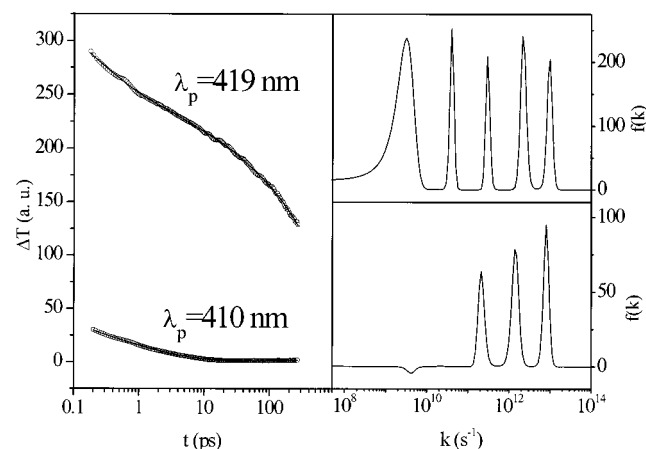
FIGURE 3: Pump-induced intensity changes (small circles) observed following photolysis of native horse heart $Mb^{3+}NO$ at room temperature, monitored at 410 and 419 nm. The solid lines are MEM fits. At 410 nm, close to the isosbestic point between the 6-coordinate NO-bound species and the transient 5-coordinate photoproduct, there is no significant absorbance change other than a sub-10 ps decay due to repopulation of the electronic ground state and cooling. The right-hand panels display the corresponding MEM rate distribution $f(\log k)$.

Table 1: Decay Time Constants from Ultrafast Measurements on Native Horse Heart Mb^{3+}

	τ_1 (ps)	τ_2 (ps)	τ_3 (ps)	τ_4 (ps)
$Mb^{3+}NO$ (measured at 410 nm)	0.7	4.6	46	270
$Mb^{3+}NO$ (measured at 419 nm)	0.6	3.9	24	320

small fraction of the $Mb^{3+}NO$ sample, might also contribute to the 24 ps component. We cannot exclude the possibility of more exotic photochemistry, such as photoinduced linkage isomerism, although this intriguing process has so far only been observed for a small fraction of nitrosyl porphyrins in the *ferrous* state at low temperature (*42*). However, the ultrafast measurements in Figure 3 confirm that the population of photochemical transients is negligible on the nanosecond time scale of the measurements in Figure 2. In particular, only the trailing edge of the geminate NO rebinding process will contribute to the nanosecond kinetics at 419 nm. Moreover, the negligible amplitude of the 300 ps process at 410 nm confirms that this wavelength is close to the isosbestic point between the 6-coordinate bound species $Fe^{3+}NO$ and the transient 5-coordinate photoproduct, consistent with our interpretation of the initial increase in ΔA at 410 nm (Figure 2b) as the appearance of a new (6-coordinate) H_2O-bound species.

As a further test of our hypothesized 3-state model, we repeated the measurement under the same conditions, using the H64L mutant of sperm whale Mb. This mutant is 5-coordinate in the Fe^{3+} state, and there is no water molecule inside the heme pocket or bound to the heme (*8*). Figure 4 shows the absorbance changes upon NO photolysis from H64L monitored again at 390, 410, and 419 nm. In contrast to native Mb, the absorbance changes are monotonic decays at all three wavelengths. This suggests that there are only two optically distinct states present during the kinetic process, which we attribute to 5-coordinate Mb^{3+} and $Mb^{3+}NO$. The absence of significant absorption changes at 410 nm upon photolysis of H64L−NO strongly supports our interpretation of the signal observed for native Mb in Figure 2b as binding and subsequent displacement of the H_2O ligand. The simpli-
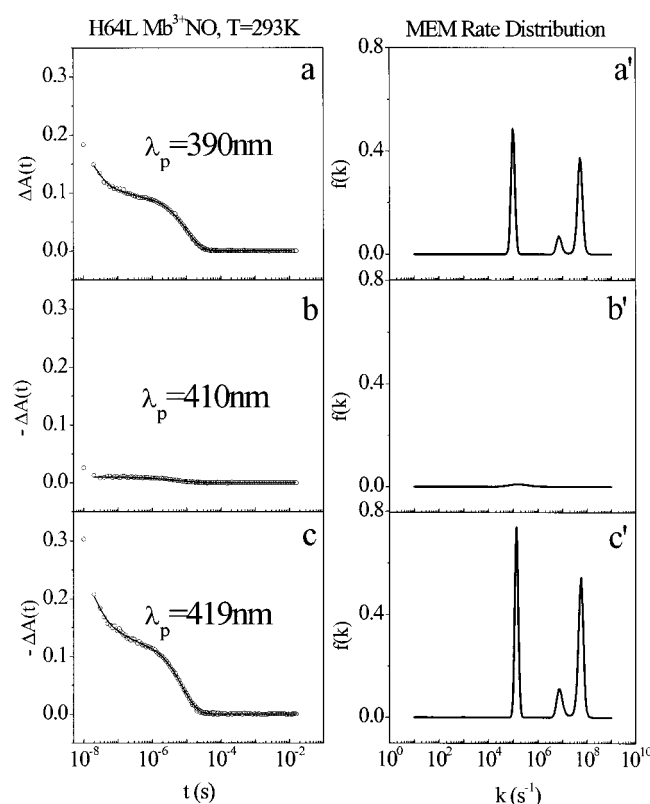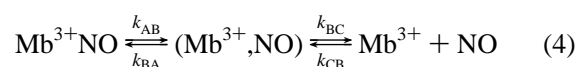

FIGURE 4: The left panels show the NO rebinding kinetics (small circles) and the MEM fit (solid lines) for ferric H64L $Mb^{3+}NO$ at 293 K, monitored at (a) 390 nm, (b) 410 nm, and (c) 419 nm. The right panels show the corresponding MEM rate distribution $f(\log k)$. In contrast to the native protein (Figure 2), the absorption change is monotonic at all wavelengths, and little absorbance change is observed at the 410 nm $Mb^{3+}NO/Mb^{3+}$ isosbestic wavelength.

fied consecutive reaction scheme

$$Mb^{3+}NO \underset{k_{BA}}{\overset{k_{AB}}{\rightleftharpoons}} (Mb^{3+},NO) \underset{k_{CB}}{\overset{k_{BC}}{\rightleftharpoons}} Mb^{3+} + NO \qquad (4)$$

can be used to interpret the kinetic phenomena for the H64L sample. In addition, comparison of Figure 2 and Figure 4 reveals that the bimolecular rebinding rate of NO to H64L mutant Mb^{3+} ($\approx 10^5$ s^{-1}) is more than 3 orders of magnitude faster than for native Mb^{3+}.

Experiments on the NO complex of H64G under identical conditions are shown in Figure 5. This mutant has a solvent molecule bound to the ferric heme (*8*), but the transient absorbance at 410 nm (Figure 5b) indicates that k_w is at least an order of magnitude faster than in native Mb. Moreover, comparison of Figure 4 and Figure 5 reveals that the bimolecular NO rebinding rate ($\sim 10^5$ s^{-1}) is almost the same for both the H64L and H64G mutants.

Fitting the experimental data in Figure 2 yields values for the rates in eq 1. Table 2 presents the temperature dependence of the rate k_w associated with water entry and binding along with the bimolecular NO rebinding rate, k_s, extracted using both MEM and LS methods. The LS analysis supplements eq 1 with an additional exponential term to fit the minor bimolecular process visible near 10^5 s^{-1} in the native Mb. To evaluate possible mechanisms for water penetration into Mb, we compare the Arrhenius barrier height associated with water entry into the heme pocket with the barrier for CO escape from ferrous Mb. In Figure 6, we display Arrhenius
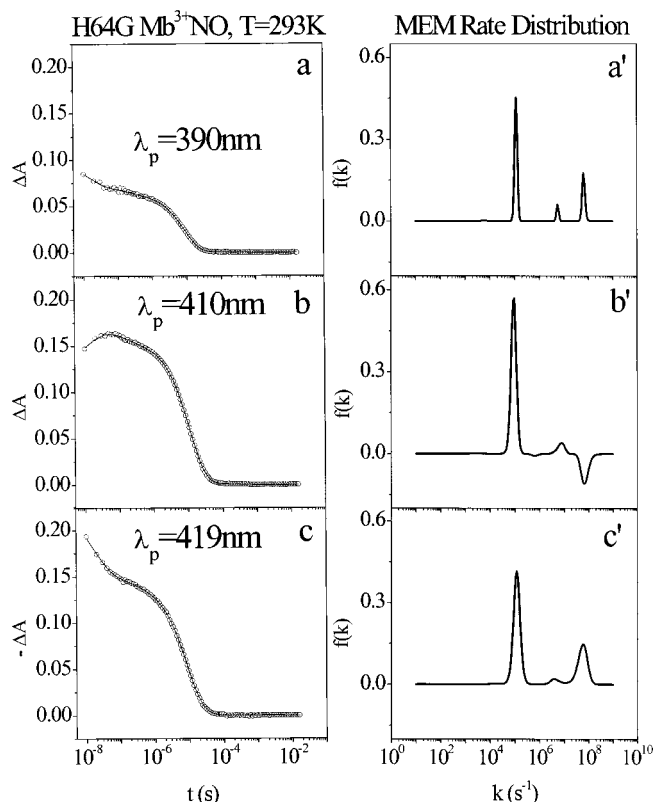
FIGURE 5: The left panels display absorbance changes (small circles) and MEM fits (solid lines) following photolysis for ferric H64G $Mb^{3+}NO$ at 293 K, monitored at (a) 390 nm, (b) 410 nm, and (c) 419 nm. The right panels show the corresponding MEM rate distribution $f(\log k)$.

Table 2: Temperature Dependence of k_w and k_s in Native Mb Obtained Using the MEM and LS Fitting Methods, along with the Rates for H64L and H64G at 293 K

temp, T (K)	k_w (s^{-1})	$k_s[NO]^{-1}$ (s^{-1} M^{-1})	$[NO]$ $(10^{-3}$ M$)^a$
293	5.7×10^6	5.6×10^4	2.0
288	4.3×10^6	4.1×10^4	2.2
283	3.7×10^6	2.3×10^4	2.5
278	2.4×10^6	1.4×10^4	2.8
273	1.6×10^6	0.7×10^4	3.2
293 (H64L)	b	5.9×10^7	2.0
293 (H64G)	6.7×10^7	4.7×10^7	2.0

^{a} Calculated from published NO solubilities (75). ^{b} Not observed.

plots both of k_w for $Mb^{3+}NO$ from Table 2, and of the rate k_{out} for CO escape from native ferrous horse heart $Mb^{2+}CO$. The latter rate is determined according to $k_{out} = k_g I_s/(I_s + I_g)$, from the rate k_g and amplitude I_g of the geminate CO rebinding rate and the amplitude I_s of bimolecular CO rebinding. Fits of data in Figure 6 to the Arrhenius relation

$$k = k_0 \exp\left(-\frac{H}{k_B T}\right) \qquad (5)$$

yield the activation enthalpy, H, and the prefactor, k_0, for the water binding rate k_w and CO escape rate k_{out}. Within experimental error, the activation enthalpies determined from the slope of the Arrhenius plot for these two processes are the same. The significance of the small vertical offset responsible for the different prefactor for these processes is unclear, because of the possibility that the rate constant determined from the LS fit to a stretched exponential may
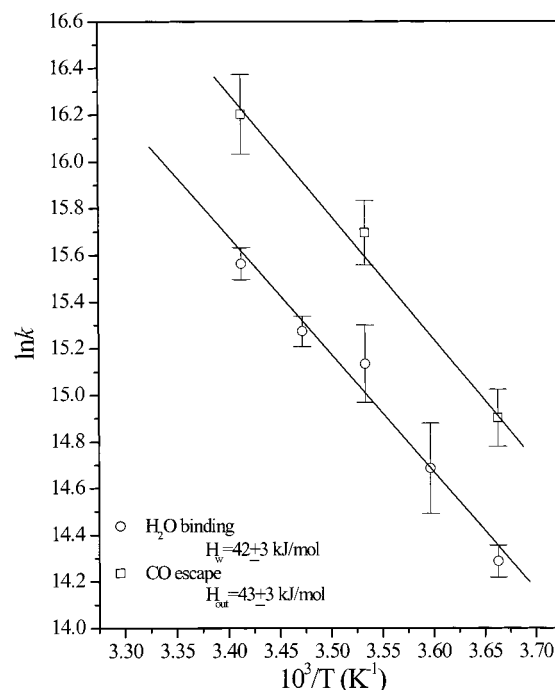

FIGURE 6: Temperature dependence of the water binding rate k_w (○) in ferric native horse heart $Mb^{3+}NO$ and the CO escape rate k_{out} (□) in ferrous native horse heart $Mb^{2+}CO$.

Table 3: Arrhenius Barrier Height and Prefactor for Water Binding (k_w) in Ferric $Mb^{3+}NO$, for CO Escape (k_{out}) in Ferrous Horse Heart $Mb^{2+}CO$, and for NO Association in Ferric $Mb^{3+}NO$

	barrier height, H (kJ/mol)	prefactor, k_0 (s^{-1})
k_w (native $Mb^{3+}NO$)	42 ± 3	2×10^{14}
k_{out} (native $Mb^{2+}CO$)	43 ± 3	7×10^{14}
k_s (native $Mb^{3+}NO$)	66 ± 5	

systematically overestimate the underlying rate (see inset in Figure 2a'). Table 3 summarizes parameters that describe the temperature dependence of observed processes.

ANALYSIS AND DISCUSSION

Kinetic Analysis for Native $Mb^{3+}NO$. For native Mb^{3+}-NO, the experimental data in Figure 2 can be fitted to several single exponential decays, using either MEM or LS methods. The rate constants for the major processes are denoted by k_g (geminate NO rebinding), k_w (bimolecular H_2O association), and k_s (bimolecular NO rebinding to Mb^{3+}), as shown in eq 1. To relate the fundamental rates in the 5-state model (eq 3) to the observed rates (eq 1), we need to solve the set of differential equations

$$\frac{dA}{dt} = -k_{AB}A + k_{BA}B$$

$$\frac{dB}{dt} = k_{AB}A - (k_{BA} + k_{BC})B + k_{CB}C$$

$$\frac{dC}{dt} = k_{BC}B - (k_{CB} + k_{CD})C + k_{DC}D \qquad (6)$$

$$\frac{dD}{dt} = k_{CD}C - (k_{DC} + k_{DE})D + k_{ED}E$$

$$\frac{dE}{dt} = k_{DE}D - k_{ED}E$$

for the initial condition $B = 1$ that exists immediately following the photolysis pulse. Here A, B, C, D, and E represent the populations of $Mb^{3+}NO$, (Mb^{3+},NO), Mb^{3+}, (Mb^{3+},H_2O), and $Mb^{3+}H_2O$, respectively. Based on the assumptions $k_{BA}, k_{BC} \gg k_{AB}, k_{CB}$ and $k_{DE}, k_{DC} \gg k_{ED}, k_{CD}$, we invoke an adiabatic time scale separation into two nearly independent sets of equations.

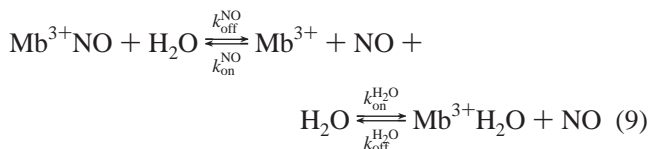The fastest time scale processes can be described by a reduced model

$$Mb^{3+}NO + H_2O \xleftarrow{k_{BA}} (Mb^{3+},NO) + H_2O \xrightarrow{k_{BC}}$$
$$Mb^{3+} + NO + H_2O \quad (7)$$
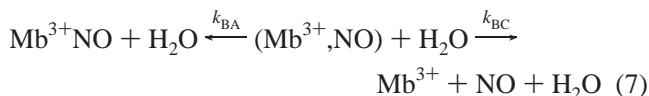
where only A, B, and C have significant populations. According to eq 7, almost all of the initial population $B = 1$ decays to A and C at a rate

$$k_g = k_{BA} + k_{BC} \quad (8)$$

From Figure 3, most of the B-state population decays on a time scale less than 1 ns, with only a small tail extending out to the nanosecond and longer time scales probed in Figure 2.

Due to the time scale separation, B and D have negligible populations at longer times, and only three states remain in the reduced equation set

$$Mb^{3+}NO + H_2O \underset{k_{on}^{NO}}{\overset{k_{off}^{NO}}{\rightleftharpoons}} Mb^{3+} + NO +$$
$$H_2O \underset{k_{off}^{H_2O}}{\overset{k_{on}^{H_2O}}{\rightleftharpoons}} Mb^{3+}H_2O + NO \quad (9)$$

where

$$k_{off}^{NO} = \frac{k_{AB} k_{BC}}{k_{BC} + k_{BA}}$$

$$k_{on}^{NO} = \frac{k_{CB} k_{BA}}{k_{BC} + k_{BA}}$$

$$k_{off}^{H_2O} = \frac{k_{ED} k_{DC}}{k_{DC} + k_{DE}}$$

$$k_{on}^{H_2O} = \frac{k_{CD} k_{DE}}{k_{DE} + k_{DC}} \quad (10)$$

Further simplifications follow upon consideration of the equilibrium behavior. In the absence of NO, almost all proteins have H_2O bound at the heme (state E), so that we take $k_{off}^{H_2O} \ll k_{on}^{H_2O}$.

Since A is the only state with substantial equilibrium population at the NO concentration used in the present experiments, we further neglect k_{off}^{NO} in comparison with other rates, and for the nanosecond experiments we only consider the population remaining in the C state following the decay of the B state. Under these conditions, the population

$$E = E_0(e^{-k_s t} - e^{-k_w t}) \quad (11)$$

of the E state probed near 410 nm undergoes a transient

increase at a rate

$$k_w = k_{on}^{NO} + k_{on}^{H_2O} \quad (12)$$

followed by a decay at the rate

$$k_s = \frac{k_{off}^{H_2O} k_{on}^{NO}}{k_w} \quad (13)$$

Displacement of Hydrogen-Bonded H_2O Modulates NO Binding. Previous studies characterized the bimolecular phase of NO binding to ferric Mb (*29, 40, 43–49*). Our measured association rate $k_s/[NO] = 5.6 \times 10^4 \text{ s}^{-1} \text{ M}^{-1}$ at 293 K (Table 2) agrees with previous results obtained using either stopped-flow (*29, 46, 47*) or flash photolysis (*47*) methodologies. Significantly larger (*40*) or smaller (*49*) NO association rates have been reported in other studies. From the temperature dependence of the NO association rates listed in Table 2, we estimate an activation enthalpy 66 ± 5 kJ/mol (Table 3), in agreement with the 63 ± 2 kJ/mol value reported by Laverman et al. (*49*).

The rate of bimolecular NO association to the ferric H64L and H64G mutants summarized in Table 2 is approximately 3 orders of magnitude faster than observed for native Mb^{3+}. The rate enhancement for H64L can be attributed to the absence of a water molecule coordinated to the heme Fe^{3+}. In the kinetic model outlined in the previous section, the presence of the bound water molecule retards NO association with the native protein by a factor $k_{off}^{H_2O}/k_w$ (eq 13) compared to NO association with a protein with a 5-coordinated heme. Indirect supporting evidence that water dissociation is a prerequisite for NO association comes from the large activation volume recently reported for this process (*49*). A water dissociation mechanism was also proposed (*43*) for NO binding to a water-soluble Fe^{3+} porphyrin model system, based on the similarity of the reported activation enthalpies for H_2O exchange (*50*) (57 kJ/mol) and NO association (*48*) (62 kJ/mol).

Although the X-ray structure of the H64G mutant (*8*) shows a solvent molecule bound to the heme Fe^{3+}, the NO association rate $k_{on} = 4.7 \times 10^7 \text{ s}^{-1} \text{ M}^{-1}$ (Table 2) is nearly as fast as for H64L. Similarly, the rate constant $k_{on} = 2.2 \times 10^7 \text{ s}^{-1} \text{ M}^{-1}$ reported for NO binding at 293 K to elephant Mb^{3+}, in which the distal His is replaced by Gln, is 500–1000 times faster than for globins with His in the E7 position (*46*), although NMR results (*51*) indicate the presence of a water bound to the heme in elephant Mb^{3+}. These results demonstrate that the bound water does not significantly impede NO binding unless it is stabilized by hydrogen bonding with the distal histidine.

To consider the possible physiological significance of this destabilization of NO binding, we may use the reported NO dissociation rate of 14 s^{-1} at 293 K (*29, 46*) to estimate a 250 μM NO dissociation constant for native Mb^{3+}. As a result, the dominant "closed pocket" conformation of oxidized Mb will have no influence on physiological signaling processes, where the peak NO concentration is expected to be in the range of 100–500 nM (*52*). Since it has been recently questioned whether Mb plays an essential role in O_2 transport (*53*), it is worth pointing out that properties of the cellular microenvironment, such as reduced pH, that favor

Table 4: Estimated Water On Rate $k_{on}^{H_2O}$, Water Off Rate $k_{off}^{H_2O}$, and Water Dissociation Constant $K = k_{off}^{H_2O}/k_{on}^{H_2O}$ at 293 K

$k_{on}^{H_2O}$ (s^{-1} M^{-1})	$k_{off}^{H_2O}$ (s^{-1})	K (mM)
1×10^5	6300	61

the "open" pocket (A_0) conformation (in which the distal His is displaced from the heme pocket and no longer available to stabilize the bound water) might allow Mb^{3+} to become a significant reservoir for NO at physiologically relevant concentrations.

An interesting contrast is provided by the heme protein nitrophorin, which transports and releases NO to facilitate the feeding of the blood-sucking bug *Rhodnius prolixus*. The 300 nM NO dissociation constant reported (*45*) for nitrophorin enables the transport and release of NO at concentrations that are believed to lead to significant vasodilation in the host animal. Although the X-ray structure of nitrophorin shows that the ferric protein is 6-coordinate in the absence of NO, the distal heme pocket does not contain a His residue (*54, 55*), again indicating that the bound solvent molecule must be stabilized by hydrogen bonding to significantly impede NO association.

Displacement of water from the heme pocket has also been proposed to influence the binding of diatomic ligands to the reduced protein (*6, 16−18*). In native Mb^{2+}, H$_2$O does not bind to the ferrous heme, but is hydrogen bonded to the distal His and is displaced on binding a sixth ligand to the heme (*8*). However, the effect on binding rates is less dramatic than that reported here for the ferric protein. For example, the rate constant for CO (O$_2$) association with H64L, which has no distal pocket water in its X-ray structure (*8*), is 50 (*6*) times faster than with the native protein (*16, 17, 56*). The influence of the distal pocket water on ligand binding to Mb^{2+} has recently been questioned (*19*) on the basis of 1.15 Å crystal structures of Mb^{2+} at room temperature (*19*) and at 100 K (*57*), which estimate approximately 50% occupancy of the distal water site.

Entry, Binding, and Dissociation of H$_2$O. Experimental data for the H64L mutant at 293 K in Figure 4 yield $k_{on}^{NO} \approx 10^5$ s^{-1}, while results on the native protein (Figure 2) yield $k_w = 5.7 \times 10^6$ s^{-1}, so we assume $k_{on}^{NO} \ll k_w$ for the native protein, and conclude from eq 12 that

$$k_w \approx k_{on}^{H_2O} \qquad (14)$$

Thus, the values reported in Table 2 for k_w represent direct measurements of the rate of water binding to ferric Mb. Moreover, assuming that the rate k_{on}^{NO} of NO binding to the 5-coordinate state has the same value for the native protein as for H64L, we can estimate from eq 13 that

$$k_s \approx \frac{k_{off}^{H_2O}}{57} \qquad (15)$$

so that the NO bimolecular rebinding rate $k_s = 110$ s^{-1} yields an estimate $k_{off}^{H_2O} = 6300$ s^{-1} (see Table 4) for the rate of H$_2$O dissociation from native Mb^{3+}H$_2$O at 293 K.

We further estimate the dissociation constant $K = 61$ mM (Table 4) for the heme-bound H$_2$O from the ratio of the off and on rates at 293 K. This value ensures 100% occupancy of the heme Fe binding site of the native protein in aqueous

solution ([H$_2$O] = 55 M) and also emphasizes the stabilizing influence of His-64 on H$_2$O binding. The absence of a bound water in the H64L mutant implies that substitution of Leu for His-64 increases the water dissociation constant by more than 3 orders of magnitude, consistent with the effect of His-64 on NO binding discussed above. The stabilization of H$_2$O binding to Mb^{3+} by His-64 parallels the influence of His-64 on O$_2$ binding to Mb^{2+}. Displacement of His-64 from the heme pocket in the open conformation dramatically increases the rate of O$_2$ dissociation (*33*), and systematic site-directed mutagenesis studies show that hydrogen bonding of O$_2$ with the distal His enhances the O$_2$ affinity of Mb^{2+} by at least 2 orders of magnitude (*17*).

Experimental results on NO binding to H64G (Figure 5) suggest the relative importance of the rates for H$_2$O entry and binding [k_{CD} and k_{DE}, respectively, in the expression (eq 10) for $k_{on}^{H_2O}$] on the observed rate $k_{on}^{H_2O} \approx k_w$ for the native protein. In H64G, H$_2$O binds to the ferric heme iron, as in native Mb. However, crystal structures of H64G, both in the CO and in the aquomet forms, show an enlarged distal pocket that is more accessible to solvent. In particular, solvent molecules are observed adjacent to the coordinated CO ligand (*8*). Upon photolysis of H64G−NO, it is thus likely that the photolyzed NO is replaced by an H$_2$O molecule that is already present in the distal pocket, rather than by a bulk solvent molecule that has to first enter the pocket, i.e., $k_w \approx k_{DE}$ for H64G. As noted above, k_w is at least 1 order of magnitude larger for H64G than for native Mb, consistent with this scenario (i.e., $k_{DE} \gg k_{DC}$ for native Mb). An important corollary is that a H$_2$O molecule entering the heme pocket of native metMb has a high probability of binding to the iron without escaping. We conclude that the H$_2$O binding rate k_w observed following photolysis of native Mb^{3+}NO is approximately equal to the rate of H$_2$O entry into the heme pocket, i.e., $k_w \approx k_{CD}$ from eqs 10 and 14 with $k_{DE} \gg k_{DC}$.

Other Measurements of H$_2$O Kinetics. The present determination of the H$_2$O binding rate supports a previous qualitative conclusion (*47*) that H$_2$O binding to photolyzed Mb^{3+}NO is complete before the beginning of the bimolecular phase of NO rebinding. A similar process presumably follows photolysis of Mb^{2+}CO, since a water molecule observed in the X-ray structure of deligated Mb^{2+} is displaced upon binding CO (*8*). Binding of H$_2$O in the distal pocket was suggested to contribute to transient changes in the visible absorption and magnetic optical rotatory dispersion signals observed following photolysis of Mb^{2+}CO on a 400−600 ns time scale (*18*), similar to that determined here for Mb^{3+}. However, the relatively weak nonbonded interaction of the distal H$_2$O molecule with the ferrous heme renders it difficult to distinguish this process from conformational changes in the heme environment for Mb^{2+}.

A recent investigation of H$_2$O kinetics in Mb was performed following reduction of Mb^{3+}H$_2$O by either irradiation or dye-mediated photoreduction at low temperatures (*22−24*). In this cryogenically stabilized Mb^{2+}H$_2$O intermediate, H$_2$O can be reversibly photolyzed, and geminate H$_2$O rebinding to the heme is governed by a distribution of barrier heights very similar to those found for diatomic heme ligands (*22*). The specific structural changes that promote dissociation of H$_2$O upon relaxation to the equilibrium Mb^{2+} structure remain unclear, although we speculate that tau-

Table 5: Water Exchange Kinetics in Biological Systems, Model Compounds, and Metal Ions

	k (s^{-1})	H (kJ/mol)
Mb (this paper)	6.3×10^3 (293 K)	b
BPTI (*58*)	5.9×10^3 (300 K)	90^a
ribonuclease A (*76*)	1.3×10^8 (300 K)	43
ribonuclease T1 (*77*)	1.4×10^8 (300 K)	b
B-DNA (*78–80*)	1×10^8 (253−277 K)	52
photosystem II (*81*)	4.9 slow component (293 K)	78
	56 fast component (293 K)	39
Fe^{3+}-TPPS (*50*)	1.4×10^7 (298 K)	57
Fe(OH$_2$)$_6$$^{3+}$ (*82*)	1.6×10^2 (298 K)	64

^{a} A non-Arrhenius description of the temperature dependence was proposed (*58*) as preferable. ^{b} Not determined.

tomerization of His-64 might alter the character of the His-64$\cdots$H$_2$O hydrogen bond. In the present study, solvent entry to the heme pocket limits k_w, so we do not obtain direct information about the geminate H$_2$O rebinding to the native ferric protein.

Various studies have reported exchange rates for water molecules bound to protein cavities, to model compounds, and to metal ions. Based on the estimated water on rate $k_{on}^{H_2O}$ and water off rate $k_{off}^{H_2O}$ listed in Table 4, we estimate the water exchange rate as approximately 6300 s^{-1} for native horse Mb^{3+}H$_2$O. Table 5 lists water exchange rates and Arrhenius barriers determined for individual water molecules bound to proteins and nucleic acids near room temperature. Most of these results have been reviewed by Halle (*9*). Since the rates span many orders of magnitude, it is likely that the mechanism of water exchange varies significantly among these cases. It is thus unexpected that the 6300 s^{-1} water exchange rate estimated here for Mb^{3+}H$_2$O is similar to the rate determined (*58*) for a buried H$_2$O in the 58-residue protein bovine pancreatic trypsin inhibitor (BPTI) (Table 5). In the case of BPTI, it has been proposed that exchange of the buried water molecule requires a large transient conformational change in the protein (*58*).

Small Molecule Access to the Active Site. The function of many proteins relies on the access of small molecules such as water or oxygen to sites in the protein interior. The solvent inaccessibility of the active site in the static structural model of myoglobin derived from X-ray diffraction measurements is a classic illustration of the importance of protein dynamics. Conformational fluctuations must open a transient pathway or pathways for entry and exit of oxygen. Based on examination of the early X-ray structures, Perutz and Chance noticed that rotation of His-64 about the C$_\alpha$−C$_\beta$ bond displaced the imidazole ring from the heme pocket and proposed that this facilitated the access of oxygen and other small molecules to the active site (*59, 60*). Early theoretical analysis (*61*) provided some support for this proposal, but later simulations identified multiple energetically accessible pathways for ligand migration between the heme pocket and solvent (*62*). Experimental input is required to clarify which pathways are actually utilized under physiological conditions.

We previously determined the rate (1.4×10^6 s^{-1}) of interconversion between "open" and "closed" pocket conformations of Mb^{2+} in aqueous pH 5 buffer at 273 K and found it to be comparable to the rate of CO escape from the distal heme pocket of the closed conformation (*34*). These rates also agree with the water entry rate at 273 K (Table

2). The crystal structure of the open conformation shows His-64 displaced from the pocket (*63*), analogous to the transient structure proposed by Perutz and Chance (*59, 60*). Together with the predominance of ligand escape through the classical pathway in simulations in which His-64 is displaced from the pocket (*62*), this suggests that ligand escape occurs primarily along the classical pathway under these solution conditions.

To our knowledge, there has not been a direct investigation of a second aspect of the Perutz/Chance hypothesis (*59, 60*), namely, that motion of His-64 facilitates ligand *entry*, as well as exit. Figure 6 compares the temperature dependence of the rates for H$_2$O binding to Mb^{3+} and CO escape from Mb^{2+} as a function of temperature. Within experimental uncertainty, the activation enthalpy is the same. This result is not an obvious consequence of most models in which small molecules migrate along multiple pathways between the heme pocket and solvent. In general, two factors would contribute to differing temperature dependences: (1) Different energies for noncovalent CO and H$_2$O binding to the heme pocket or other internal cavities would cause these molecules to migrate through the protein matrix at different rates. (2) Even in the absence of molecule-specific migration rates, differences in the energy of molecular binding in the pocket rather than in solvent should lead to nonequivalent rates for exit and entry.

On the other hand, a model in which transient formation of an "open" conformation drastically lowers the barrier for small molecule migration between the heme pocket and solvent provides a natural explanation for the results in Figure 6. In this case, the rate-limiting step is the same for exit and entry and is independent of the migrating molecule, and the activation enthalpy determined from the slope of Figure 6 is the barrier to formation of the open conformation. Interestingly, a similar model was proposed to describe quenching of Zn-substituted Mb fluorescence by oxygen (*64*). However, that study reported a 14.5 kJ/mol value for the activation enthalpy associated with the O$_2$ exit process, much smaller than the 42 kJ/mol value determined here for CO escape. Comparison of these results suggests that the quenching site is distinct from the binding site, and that more limited conformational changes enable migration between the quenching site and the solvent.

While the evidence presented here further supports ligand entry and exit via a common pathway controlled by displacement of His-64 from native Mb in aqueous solution, other pathways may be accessed in Mb mutants or in nonaqueous solutions. In 75% glycerol solutions, we and others previously determined a rate of open/closed interconversion (*34, 65, 66*) that is at least an order of magnitude slower than the rate of CO escape. In this case, the dramatic reduction of the interconversion rate in the highly viscous solution forces the ligand to find alternative pathways to the solvent. Time-resolved studies of the H64Y mutant led to the conclusion that Tyr-64 is displaced from the pocket on a millisecond time scale, approximately 3 orders of magnitude slower than the displacement of His-64 from the native protein (*67*). Again, this would presumably force the ligand to escape by an alternative pathway. The dominant escape pathway(s) for ligand escape also varies (vary) in molecular dynamics simulations. Simulations starting from the closed conformation reveal multiple energetically accessible path-

ways for ligand escape. On the other hand, most ligands escape via the classical pathway during the course of 100 ps simulations in which His-64 is displaced from the heme pocket (*62*).

Recently reported structures (*68–70*) of native and mutant MbCO crystals following CO photolysis find that, as previously suggested (*71*), extended illumination at cryogenic temperatures results in CO migration from its original location directly above the heme to other internal cavities, including a well-characterized Xe binding site (*72*) in the *proximal* heme pocket. Since significant loss of CO population is not reported in these studies, CO apparently migrates between internal cavities on a time scale rapid compared to escape from the protein under these conditions. Time-resolved IR measurements at room temperature also suggest the transient occupation of spectrally distinct intermediate states prior to the appearance of CO in the solvent (*73*). Our conclusion that ligand escape from and entry into the protein is "gated" by His-64 is not inconsistent with these results. One plausible scenario in aqueous solution would involve relatively rapid equilibration of the photolyzed ligand among internal cavities, followed by ligand escape during a transient excursion to the open conformation. A similar conclusion results from a recent analysis of the effects of site-directed mutagenesis on O_2 rebinding (*74*).

CONCLUSION

The findings presented above on the penetration and binding of water to the active site of ferric myoglobin illuminate the dual role of His-64 in stabilizing ligand binding at the heme and controlling access to the protein interior. Strongly enhanced NO association rates for position 64 mutants suggest that hydrogen bonding of the heme-bound H_2O with His-64 impedes NO binding to ferric myoglobin. The observed rate for water entry and binding to native Mb is $k_w \approx 5.7 \times 10^6$ s^{-1} at 293 K, and the barrier height is $H_w = 42$ kJ/mol. We previously noted that the rates for open/closed interconversion and CO escape were the same at pH 5 for sperm whale Mb (*34*), consistent with CO escape along the classical pathway gated by His-64. The nearly identical barriers observed here for water entry and CO escape at neutral pH strongly support a common His-64 gated pathway for exit and entry of small molecules.

REFERENCES

1. Sage, J. T., and Champion, P. M. (1996) in *Comprehensive Supramolecular Chemistry* (Suslick, K. S., Ed.) pp 171–218, Pergamon Press, Oxford, U.K.
2. Jia, L., Bonaventura, C., Bonaventura, J., and Stamler, J. S. (1996) *Nature 380*, 221–226.
3. Ignarro, L. J., Cirino, G., Casini, A., and Napoli, C. (1999) *J. Cardiovasc. Pharmacol. 34*, 879–886.
4. Snyder, S. H., and Bredt, D. S. (1992) *Sci. Am. 266*, 68–77.
5. Garthwaite, J., and Boulton, C. L. (1995) *Annu. Rev. Physiol. 57*, 683–706.
6. Olson, J. S., and Phillips, G. N., Jr. (1996) *J. Biol. Chem. 271*, 17593–17596.
7. Antonini, E., and Brunori, M. (1971) *Hemoglobin and myoglobin in their reactions with ligands*, North-Holland Publishing Co., Amsterdam and London.
8. Quillin, M. L., Arduini, R. M., Olson, J. S., and Phillips, G. N., Jr. (1993) *J. Mol. Biol. 234*, 140–155.
9. Halle, B. (1999) in *Hydration Processes in Biology: Theoretical and Experimental Approaches* (Bellisent-Funel, M. C., Ed.) pp 233–259, IOS Press, Amsterdam.
10. Denisov, V. P., Jonsson, B.-H., and Halle, B. (1999) *J. Am. Chem. Soc. 121*, 2327–2328.
11. Silverman, D. N., and Lindskog, S. (1988) *Acc. Chem. Res. 21*, 30–36.
12. Silverman, D. N. (1995) *Methods Enzymol. 249*, 479–503.
13. Gu, M., and Schoenborn, B. P. (1995) *Proteins: Struct., Funct., Genet. 22*, 20–26.
14. García, A. E., and Hummer, G. (2000) *Proteins: Struct., Funct., Genet. 38*, 261–272.
15. Helm, L., and Merbach, A. E. (1999) *Coord. Chem. Rev. 187*, 151–181.
16. Rohlfs, R. J., Mathews, A. J., Carver, T. E., Olson, J. S., Springer, B. A., Egeberg, K. D., and Sligar, S. G. (1990) *J. Biol. Chem. 265*, 3168–3176.
17. Springer, B. A., Sligar, S. G., Olson, J. S., and Phillips, G. N., Jr. (1994) *Chem. Rev. 94*, 699–714.
18. Esquerra, R. M., Goldbeck, R. A., Kim-Shapiro, D. B., and Kliger, D. S. (1998) *Biochemistry 37*, 17527–17536.
19. Kachalova, G. S., Popov, A. N., and Bartunik, H. D. (1999) *Science 284*, 473–476.
20. Christian, J. F., Unno, M., Sage, J. T., Champion, P. M., Chien, E., and Sligar, S. G. (1997) *Biochemistry 36*, 11198–11204.
21. La Mar, G. N., Dalichow, F., Zhao, X., Dou, Y., Ikeda-Saito, M., Chiu, M. L., and Sligar, S. G. (1994) *J. Biol. Chem. 269*, 29629–29635.
22. Lamb, D. C., Prusakov, V., Engler, N., Ostermann, A., Schellenberg, P., Parak, F. G., and Nienhaus, G. U. (1998) *J. Am. Chem. Soc. 120*, 2981–2982.
23. Lamb, D. C., Ostermann, A., Prusakov, V. E., and Parak, F. G. (1998) *Eur. Biophys. J. 27*, 113–125.
24. Engler, N., Ostermann, A., Gassmann, A., Lamb, D. C., Prusakov, V. E., Schott, J., Schweitzer-Stenner, R., and Parak, F. G. (2000) *Biophys. J. 78*, 2081–2092.
25. Springer, B. A., and Sligar, S. G. (1987) *Proc. Natl. Acad. Sci. U.S.A. 84*, 8961–8965.
26. Hoshino, M., Maeda, M., Konishi, R., Seki, H., and Ford, P. C. (1996) *J. Am. Chem. Soc. 118*, 5702–5707.
27. Kholodenko, Y., Gooding, E. A., Dou, Y., Ikeda-Saito, M., and Hochstrasser, R. M. (1999) *Biochemistry 38*, 5918–5924.
28. Miller, L. M., Pedraza, A. J., and Chance, M. R. (1997) *Biochemistry 36*, 12199–12207.
29. Sharma, V. S., Isaacson, R. A., John, M. E., Waterman, M. R., and Chevion, M. (1983) *Biochemistry 22*, 3897–3902.
30. Benko, B., and Yu, N. T. (1983) *Proc. Natl. Acad. Sci. U.S.A. 80*, 7042–7046.
31. Morikis, D., Champion, P. M., Springer, B. A., and Sligar, S. G. (1989) *Biochemistry 28*, 4791–4800.
32. Tian, W. D., Sage, J. T., Šrajer, V., and Champion, P. M. (1992) *Phys. Rev. Lett. 68*, 408–411.
33. Tian, W. D., Sage, J. T., and Champion, P. M. (1993) *J. Mol. Biol. 233*, 155–166.
34. Tian, W. D., Sage, J. T., Champion, P. M., Chien, E., and Sligar, S. G. (1996) *Biochemistry 35*, 3487–3502.
35. Rosca, F., Kumar, A. T. N., Ye, X., Sjodin, T., Demidov, A. A., and Champion, P. M. (2000) *J. Phys. Chem. 104*, 4280–4290.
36. Kumar, A. T. N., Zhu, L., Christian, J. F., and Champion, P. M. *J. Phys. Chem. B*, submitted for publication.
37. Livesey, A. K., and Brochon, J. C. (1987) *Biophys. J. 52*, 693–706.
38. Skilling, J., and Bryan, R. K. (1984) *Mon. Not. R. Astron. Soc. 211*, 111–124.
39. Morikis, D., Champion, P. M., Springer, B. A., Egeberg, K. D., and Sligar, S. G. (1990) *J. Biol. Chem. 265*, 12143–12145.
40. Hoshino, M., Ozawa, K., Seki, H., and Ford, P. C. (1993) *J. Am. Chem. Soc. 115*, 9568–9575.

41. Kobayashi, K., Tamura, M., Hayashi, K., Hori, H., and Morimoto, H. (1980) *J. Biol. Chem. 255*, 2239−2242.

42. Cheng, L., Novozhilova, I., Kim, C., Kovalevsky, A., Bagley, K. A., Coppens, P., and Richter-Addo, G. B. (2000) *J. Am. Chem. Soc. 122*, 7142−7143.

43. Hoshino, M., Laverman, L., and Ford, P. C. (1999) *Coord. Chem. Rev. 187*, 75−102.

44. Ford, P. C., Bourassa, J., Miranda, K., Lee, B., Lorkovic, I., Boggs, S., Kudo, S., and Laverman, L. (1998) *Coord. Chem. Rev. 171*, 185−202.

45. Kaneko, Y., Yuda, M., Iio, T., Murase, T., and Chinzei, Y. (1999) *Biochim. Biophys. Acta 1431*, 492−499.

46. Sharma, V. S., Traylor, T. G., Gardiner, R., and Mizukami, H. (1987) *Biochemistry 26*, 3837−3843.

47. Kobayashi, K., Tamura, M., and Hayashi, K. (1982) *Biochemistry 21*, 729−732.

48. Laverman, L. E., Hoshino, M., and Ford, P. C. (1997) *J. Am. Chem. Soc. 119*, 12663−12664.

49. Laverman, L. E., Wanat, A., Oszajca, J., Stochel, G., Ford, P. C., and van Eldik, R. (2001) *J. Am. Chem. Soc. 123*, 285−293.

50. Ostrich, I. J., Liu, G., Dodgen, H. W., and Hunt, J. P. (1980) *Inorg. Chem. 19*, 619−621.

51. Krishnamoorthi, R., La Mar, G. N., Mizukami, H., and Romero, A. (1984) *J. Biol. Chem. 259*, 265−270.

52. Malinski, T., and Taha, Z. (1992) *Nature 358*, 676−678.

53. Garry, D. J., Ordway, G. A., Lorenz, J. N., Radford, N. B., Chin, E. R., Grange, R. W., Bassel-Duby, R., and Williams, R. S. (1998) *Nature 395*, 905−908.

54. Andersen, J. F., Weichsel, A., Balfour, C. A., Champagne, D. E., and Montfort, W. R. (1998) *Structure 6*, 1315−1327.

55. Weichsel, A., Andersen, J. F., Champagne, D. E., Walker, F. A., and Montfort, W. R. (1998) *Nat. Struct. Biol. 5*, 304−309.

56. Li, T., Quillin, M. L., Phillips, G. N., Jr., and Olson, J. S. (1994) *Biochemistry 33*, 1433−1446.

57. Vojtěchovský, J., Chu, K., Berendzen, J., Sweet, R. M., and Schlichting, I. (1999) *Biophys. J. 77*, 2153−2174.

58. Denisov, V. P., Peters, J., Horlein, H. D., and Halle, B. (1996) *Nat. Struct. Biol. 3*, 505−509.

59. Perutz, M. F., and Mathews, F. S. (1966) *J. Mol. Biol. 21*, 199−202.

60. Chance, B., Ravilly, A., and Rumen, N. (1966) *J. Mol. Biol. 17*, 525−534.

61. Case, D. A., and Karplus, M. (1979) *J. Mol. Biol. 132*, 343−368.

62. Elber, R., and Karplus, M. (1990) *J. Am. Chem. Soc. 112*, 9161.

63. Yang, F., and Phillips, G. N., Jr. (1996) *J. Mol. Biol. 256*, 762−774.

64. Carrero, J., Jameson, D. M., and Gratton, E. (1995) *Biophys. Chem. 54*, 143−154.

65. Young, R. D., Frauenfelder, H., Johnson, J. B., Lamb, D. C., Nienhaus, G. U., Philipp, R., and Scholl, R. (1991) *Chem. Phys. 158*, 315−327.

66. Johnson, J. B., Lamb, D. C., Frauenfelder, H., Muller, J. D., McMahon, B., Nienhaus, G. U., and Young, R. D. (1996) *Biophys. J. 71*, 1563−1573.

67. Mukai, M., Nakashima, S., Olson, J. S., and Kitagawa, T. (1998) *J. Phys. Chem. B 102*, 3624−3630.

68. Chu, K., Vojtěchovský, J., McMahon, B. H., Sweet, R. M., Berendzen, J., and Schlichting, I. (2000) *Nature 403*, 921−923.

69. Brunori, M., Vallone, B., Cutruzzolà, F., Travaglini-Allocatelli, C., Berendzen, J., Chu, K., Sweet, R. M., and Schlichting, I. (2000) *Proc. Natl. Acad. Sci. U.S.A. 97*, 2085−2063.

70. Ostermann, A., Waschipky, R., Parak, F. G., and Nienhaus, G. U. (2000) *Nature 404*, 205−208.

71. Šrajer, V., Reinisch, L., and Champion, P. M. (1991) *Biochemistry 30*, 4886−4895.

72. Tilton, R. F., Kuntz, I. D., Jr., and Petsko, G. A. (1984) *Biochemistry 23*, 2849−2857.

73. Lim, M., Jackson, T. A., and Anfinrud, P. A. (1997) *Nat. Struct. Biol. 4*, 209−214.

74. Scott, E. E., Gibson, Q. H., and Olson, J. R. (2001) *J. Biol. Chem. 276*, 5177−5188.

75. Seidell, A. (1940) *Solubilities of inorganic and metal organic compounds; a compilation of quantitative solubility data from the periodical literature*, D. Van Nostrand Co., Inc., New York.

76. Denisov, V. P., and Halle, B. (1998) *Biochemistry 37*, 9595−9604.

77. Langhorst, U., Loris, R., Denisov, V. P., Doumen, J., Roose, P., Maes, D., Halle, B., and Steyaert, J. (1999) *Protein Sci. 8*, 722−730.

78. Phan, A. T., Leroy, J.-L., and Guéron, M. (1999) *J. Mol. Biol. 286*, 505−519.

79. Denisov, V. P., Carlström, G., Venu, K., and Halle, B. (1997) *J. Mol. Biol. 268*, 118−136.

80. Jóhannesson, H., and Halle, B. (1998) *J. Am. Chem. Soc. 120*, 6859−6870.

81. Hillier, W., Messinger, J., and Wydrzynski, T. (1998) *Biochemistry 37*, 16908−16914.

82. Grant, M., and Jordan, R. B. (1981) *Inorg. Chem. 20*, 55−60.